

Rotation sensing with improved stability using point-source atom interferometryChen Avinadav^{1,2,*}, Dimitry Yankelev^{1,2,*}, Moshe Shuker², Ofer Firstenberg¹ and Nir Davidson¹¹*Department of Physics of Complex Systems, Weizmann Institute of Science, Rehovot 7610001, Israel*²*Rafael Ltd., Haifa 3102102, Israel*

(Received 4 March 2020; accepted 9 July 2020; published 29 July 2020)

Point-source atom interferometry is a promising approach for implementing robust, high-sensitivity, rotation sensors using cold atoms. However, its scale factor, i.e., the ratio between the interferometer signal and the actual rotation rate, depends on the initial conditions of the atomic cloud, which may drift in time and result in bias instability, particularly in compact devices with short interrogation times. We present two methods to stabilize the scale factor. One relies on a model-based correction which exploits correlations between multiple features of the interferometer output and works on a single-shot basis. The other is a self-calibrating method where a known bias rotation is applied to every other measurement, requiring no prior knowledge of the underlying model but reducing the sensor bandwidth by a factor of two. We demonstrate both schemes experimentally with complete suppression of scale-factor drifts, maintaining the original rotation sensitivity and allowing for bias-free operation over several hours.

DOI: [10.1103/PhysRevA.102.013326](https://doi.org/10.1103/PhysRevA.102.013326)**I. INTRODUCTION**

In recent years, cold-atom interferometers [1] have achieved record sensitivities in acceleration and rotation sensing. As acceleration-sensing instruments, their applications range from precision measurements for fundamental research [2–10] to geophysical measurements with mobile atomic gravimeters [11–18], demonstrating both high-sensitivity and high-stability operation. Atom interferometry gyroscopes [19–24] are useful for field applications such as gyrocompassing [25,26] and inertial navigation on mobile platforms [27–29]. Similarly to atomic and optical clocks, atomic gyroscopes hold the promise of enhanced stability compared to their classical counterparts due to their scale factor being defined in terms of fundamental physical constants. Previous demonstrations of atom interferometry gyroscopes [23,30] have reached sensitivity and stability which compare favorably with state-of-the-art optical gyroscopes [31,32].

Point-source interferometry (PSI) is an atom interferometry technique for rotation sensing based on detecting the spatial frequency of the interference pattern across an atomic cloud. Originally developed in a 10 meter atomic fountain [22], the technique has also been applied in a sensor with a cm-scale physics package [33]. Compared to other atom interferometry rotation sensing techniques, PSI has the benefits of experimental simplicity and inherent suppression of accelerations and vibrations. As such, it is an especially promising technique for field and mobile applications. However, unlike ideal atomic sensors, the scale factor of PSI, defined as the ratio between the measured spatial frequency of the fringe pattern and the applied rotation rate, is sensitive to the initial and final size of the atomic cloud [34]. This dependency is

amplified when the expansion ratio of the cloud is small, as in compact sensors with short expansion times. As a result, PSI is susceptible to bias instability due to drifts in its technical attributes [24], preventing it from realizing its full potential as an atomic sensor and limiting its usefulness in applications requiring high stability over long timescales.

In this work, we introduce two approaches to stabilizing scale-factor drifts in PSI sensors. The first approach utilizes additional information extracted from each PSI image, namely, the interference fringe contrast and atomic cloud final size, in addition to the fringe spatial frequency. We experimentally verify the physical model which describes the correlation between these parameters and then employ it to correct the scale factor independently for every PSI image. The second approach relies on alternately applying a known bias rotation rate to the sensor, in addition to the unknown measured rotation. Analyzing pairs of measurements with and without the bias rotation enables self-calibration of the scale-factor correction and determination of the unknown rotation. We implement both schemes experimentally and demonstrate their ability to recover uncorrelated $\tau^{-1/2}$ averaging performance of the rotation sensor. We achieve suppression of scale-factor drifts up to a factor of ten without any loss in sensitivity and on timescales of up to 10^4 s, far surpassing previous results.

II. POINT-SOURCE ATOM INTERFEROMETRY

PSI gyroscopes employ a Mach-Zehnder atom interferometer configuration [35]. Three laser pulses, equally separated in time, interact with a freely falling atomic cloud and act, in analogy to optical interferometry, as coherent beam splitters and mirrors. These operations are realized through counterpropagating laser beams which drive two-photon, Doppler-sensitive Raman transitions between different internal ground-state levels and different momentum states of the atom [36]. Beam-splitter operations correspond to $\pi/2$ pulses which place the atom in a coherent superposition

*These two authors contributed equally to this work.

†chen.avinadav@weizmann.ac.il

‡dimitry.yankelev@weizmann.ac.il

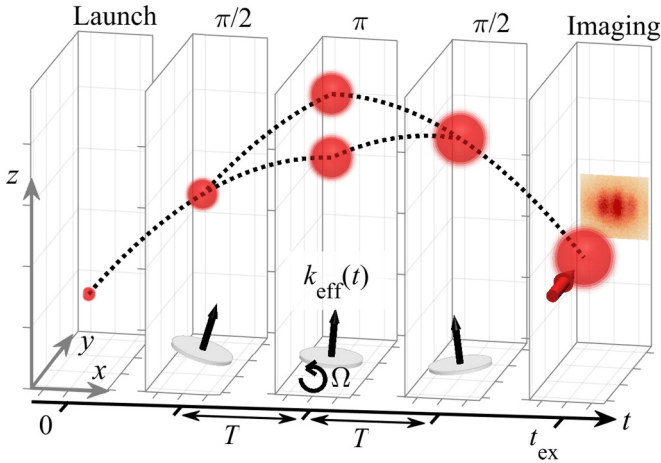


FIG. 1. Schematic diagram of point-source atom interferometry. The atomic cloud is launched upwards at $t = 0$, interacts with a sequence of $\pi/2$ - π - $\pi/2$ two-photon Raman pulses comprising the interferometer, and finally imaged at $t = t_{\text{ex}}$. The effective wave vector \mathbf{k}_{eff} of the counterpropagating Raman beams is determined by a retroreflecting mirror which can be tilted by a piezo stage to simulate rotations. Ballistic expansion of the cloud generates correlation between the position and velocity of the atoms, giving rise to a spatial interference pattern from which the rotation rate is calculated.

of two momentum states separated by $\hbar\mathbf{k}_{\text{eff}}$, where $\mathbf{k}_{\text{eff}} = \mathbf{k}_1 - \mathbf{k}_2$ is the two-photon wave vector of the Raman interaction. Likewise, mirror operations correspond to π pulses which change the momentum of each interferometer arm by $\pm\hbar\mathbf{k}_{\text{eff}}$. During the interferometer sequence, these pulses are utilized to coherently split, redirect, and recombine the atomic wave packets in space (Fig. 1). The interferometer phase ϕ results from the different spatial trajectories of the two arms, and determines the relative population in the two internal states at the interferometer output. Through state-dependent detection of the atoms, this relative population, and thus the phase, can be measured.

In the Mach-Zehnder configuration considered here, the leading phase contributions are given by $\phi_{\mathbf{a}} = (\mathbf{k}_{\text{eff}}T^2) \cdot \mathbf{a}$ and $\phi_{\Omega} = (2\mathbf{v} \times \mathbf{k}_{\text{eff}}T^2) \cdot \Omega$, where T is the time between each pair of pulses, \mathbf{a} and Ω are, respectively, the acceleration and rotation rate of the atoms relative to the interrogating Raman beams, and \mathbf{v} is the mean velocity of each atom during the interferometer sequence. The acceleration phase $\phi_{\mathbf{a}}$ can be seen as resulting from the space-time area enclosed by the two interferometer arms, whereas the rotation phase ϕ_{Ω} results from the enclosed spatial area, in a Sagnac-like effect.

While $\phi_{\mathbf{a}}$ is uniform across the expanding atomic cloud, ϕ_{Ω} depends on the initial transverse velocity of each atom due to the cloud's finite temperature. In the point-source limit, where the final cloud is much larger than its initial size, ballistic expansion of the cloud results in one-to-one correspondence between the atomic position and velocity. Thus, the velocity-dependent rotation phase is projected onto a spatial fringe pattern which may be directly imaged to facilitate a measurement of Ω [22].

In our setup, the Raman beams are aligned vertically such that $\mathbf{k}_{\text{eff}} = k_{\text{eff}}\hat{\mathbf{z}}$, and the cloud is imaged in the $\hat{\mathbf{x}}$ - $\hat{\mathbf{z}}$ plane,

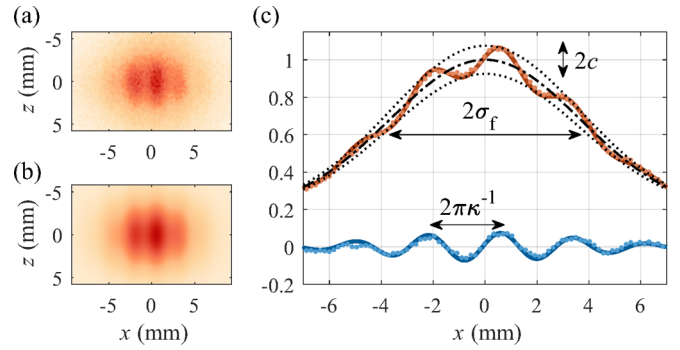


FIG. 2. Spatial fringe pattern measured with PSI. (a) Raw fluorescence image from a single experiment. (b) Fit of the image to a two-dimensional Gaussian distribution with sinusoidal modulation. (c) Normalized, vertically integrated cross sections of the measured and fitted images (red dotted and solid lines, respectively). The Gaussian density distribution (dash-dotted line) of full width $2\sigma_f$ is modulated by a fringe pattern (blue) with spatial frequency κ and contrast c . In this experiment, the initial cloud width was $2\sigma_i = 0.98$ mm (measured separately) with magnification of $\sigma_f/\sigma_i \sim 7.5$.

providing sensitivity to gravitational acceleration $-\hat{\mathbf{z}}$ and to rotations around the $\hat{\mathbf{y}}$ axis. From here on, we will focus on the latter term only. For simplicity, we denote $\Omega = \Omega_y$ and write the rotation phase as $\phi_{\Omega} = 2k_{\text{eff}}\Omega v_x T^2$. In the point-source limit, we have $x = v_x t_{\text{ex}}$, where t_{ex} is the total expansion time of the cloud, and the rotation phase becomes $\phi_{\Omega} = (2k_{\text{eff}}\Omega T^2/t_{\text{ex}})x$. The resulting atomic density has a profile of a modulated Gaussian distribution, as shown in Fig. 2, whose spatial frequency is given by $\kappa = (2k_{\text{eff}}T^2/t_{\text{ex}})\Omega$. More generally, we may write the spatial fringe frequency as $\kappa(\Omega) = F\Omega$, where F is the scale factor, given in the point-source limit by $F_{\text{ps}} = 2k_{\text{eff}}T^2/t_{\text{ex}}$ [33].

In general, realization of a rotation-sensing atom interferometry requires separating the phase contributions of rotation and acceleration. In PSI, this is achieved by exploiting the velocity dependence of the rotation-sensitive phase ϕ_{Ω} to map it onto a spatially varying interference pattern, separating rotation and acceleration into the spatial fringe frequency and phase, respectively [24]. A different approach utilizes two atomic sources with opposite velocities, using either thermal [20] or cold atoms [28], and performing identical Mach-Zehnder sequences on both. Here too, the velocity dependence of ϕ_{Ω} results in the output phases of the two interferometers to be $\phi_{\mathbf{a}} \pm \phi_{\Omega}$, allowing simple separation of the two contributions. However, unlike PSI in these schemes ϕ_{Ω} is uniform for each of the two interferometers. Alternatively, a four-pulse “butterfly” interferometry sequence [23] may be used, which inherently rejects the contribution of constant acceleration but remains sensitive to time-varying acceleration, such as vibration noise. In comparison to these two schemes, PSI offers a much simpler experimental configuration using only a single atomic source and a single interrogation optical beam, with suppression of both constant acceleration and vibrations.

III. EXPERIMENTAL APPARATUS

In our apparatus [37,38], we load an ensemble of ^{87}Rb atoms from thermal background vapor in a magneto-optical

trap (MOT) and cool them to $4\ \mu\text{K}$. Through moving optical molasses, the atoms are launched vertically with velocities of up to $1.2\ \text{m/s}$ while occupying all Zeeman states $m_F = 0, \pm 1$ of the lower hyperfine level $F = 1$. The interferometer pulses are realized by counterpropagating Raman beams with $\sigma^+ - \sigma^+$ polarizations that drive two-photon transitions between the $m_F = 0$ states of $F = 1$ and $F = 2$, with a bias magnetic field of about $300\ \text{mG}$ to separate the magnetic Zeeman states.

Raman beams are realized by phase modulation at $\sim 6.834\ \text{GHz}$ with an electro-optic modulator, with the carrier detuned $700\ \text{MHz}$ red of the $F = 2 \rightarrow F' = 1$ transition, followed by a two-stage amplification to a total power of about $1\ \text{W}$ in all sidebands. The Raman beam is collimated to $70\ \text{mm}$ diameter using a Silicon Lightwave LB80 output collimator with $\lambda/10$ wavefront error. The resulting two-photon Rabi frequency is $35\ \text{kHz}$.

The retroreflecting mirror of the Raman beams is mounted on an accurate nanopositioning tip-tilt piezo stage (nPoint RXY3-410), which allows us to rotate the optical wave vector during the interferometer sequence and thereby mimic actual rotations. The stage has total dynamic range of $\pm 1.5\ \text{mrad}$ in a closed-loop operation, with $0.2\ \mu\text{rad}$ position noise and a few milliseconds settling time.

Following the interferometer sequence, we use fluorescence excitation on the optical $F = 2 \rightarrow F' = 3$ cycling transition, employing all six MOT beams for minimal distortions, to capture an image of the atoms occupying the $F = 2$ level. From launch to detection, the experimental sequence lasts, in total, up to $300\ \text{ms}$. The shot-to-shot cycle time is $3\ \text{s}$ due to technical limitations in the communication bandwidth of the computer control system.

Images are taken on a PCO Pixelfly CCD camera, using a Fujinon-TV H6X12.5R zoom lens. We fit the image from each experiment to a Gaussian envelope function with sinusoidal modulation and extract κ , from which Ω is inferred (Fig. 2). We calibrate the imaging system by using velocity-selective Raman pulses and their well-known timing and momentum transfer, to select and image two narrow atomic ensembles at controllable distances.

IV. FINITE-SIZE EFFECTS

A. Theoretical model

For clouds of finite initial size, the resulting atomic density profile is a convolution of the initial density distribution with the ideal point-source fringe pattern, which is a spatial fringe superimposed on the unperturbed final density distribution. Mathematically, such convolution modifies both the wavelength and contrast of the fringe compared to the ideal point-source case. Hoth *et al.* derived analytically these effects assuming spherically symmetric Gaussian initial and final density distributions [34]. In this case, both the spatial fringe frequency κ and its contrast c are reduced with respect to their values in the point-source limit. Defining the initial and final cloud widths as σ_i and σ_f , respectively, the modified fringe properties were found

to be

$$\kappa = F_{\text{ps}} \Omega (1 - \sigma_i^2 / \sigma_f^2), \quad (1)$$

$$c = c_0 \exp \left[-\frac{1}{2} \frac{\kappa^2 \sigma_i^2}{1 - \sigma_i^2 / \sigma_f^2} \right], \quad (2)$$

where c_0 is the interferometer contrast for $\Omega = 0$.

In physical terms, imperfect correlation between the atoms' position and velocity due to the finite-size of the initial cloud results in averaging over atoms with different velocities at each measured position. For a Gaussian velocity distribution, the average velocity of atoms at each position is smaller than the expected value in the point-source limit, resulting in a reduction of the spatial fringe frequency. Similarly, the average over different velocities smears the interference fringes and reduces their contrast.

As a consequence of Eq. (1), the scale factor of the interferometer becomes $F = F_{\text{ps}} (1 - \sigma_i^2 / \sigma_f^2)$. The dependency on σ_i / σ_f leads to bias instability of the sensor when either σ_i or σ_f drift. Importantly, for a given relative drift in σ_i , the drift in the scale factor increases with the inverse magnification ratio σ_i / σ_f , emphasizing the susceptibility of compact sensors with small magnification to such drifts.

A larger magnification ratio can be achieved by decreasing σ_i using, e.g., tight dipole traps, which adds experimental complexity and may impact the atom number; or by increasing σ_f through longer expansion times or higher cloud temperatures, in either case requiring larger atom optics and detection beams. However, even when operating at a large magnification ratio such as $\sigma_f / \sigma_i = 50$, the scale factor is modified by $400\ \text{ppm}$ and small drifts in the initial cloud size on the order of a few percent would result in changes of tens parts per million to the scale factor. In comparison, optical gyroscopes achieve scale-factor stability of the order of $1\ \text{ppm}$ [39].

B. Experimental verification

We verify the model predictions by performing measurements with different values of σ_i , obtained through different repump intensities at the final optical molasses stage, and with different values σ_f , obtained through different launch velocities and thus different expansion times. σ_i was measured in independent experiments by imaging the cloud immediately after launch. For standard operation of the optical molasses, the value of σ_i is about $0.5\ \text{mm}$, and we can increase it up to about $0.8\ \text{mm}$ before suffering significant loss of atoms. As Fig. 3 shows, we find good agreement with the functionals in Eqs. (1) and (2) for a range of magnification ratios σ_f / σ_i between 3.5 and 9 , corresponding to changes of 5% in scale factor. The fact that the scale factor F at $\sigma_i / \sigma_f \rightarrow 0$ differs from F_{ps} by 3.5% can be attributed to imaging distortions and to residual calibration errors of the imaging system and of the piezo stage driving the mirror rotations. The fitted slope for the scale-factor dependence on σ_i^2 / σ_f^2 , as well as the scaling of the exponential decrease of the contrast, slightly differ from the theoretical model either due to estimation errors in σ_i and σ_f or due to non-Gaussian density distributions.

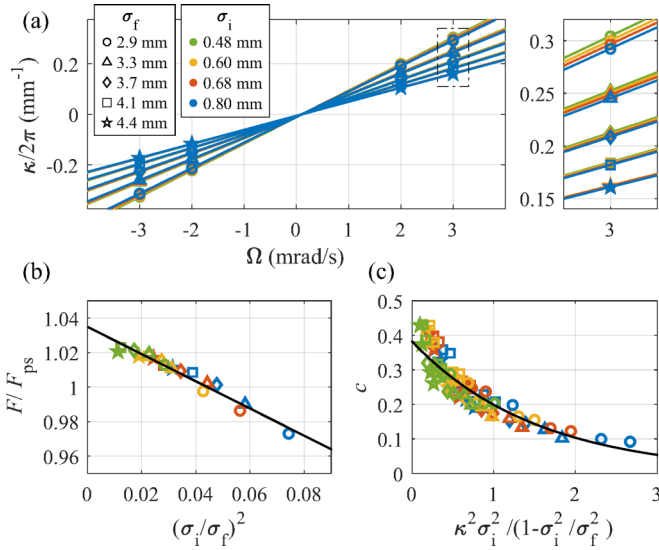


FIG. 3. Effect of initial cloud size σ_i and final cloud size σ_f on the PSI scale factor and contrast. (a) Measured spatial fringe frequency κ as a function of Ω for different values of σ_i and σ_f . Solid lines are linear fits, with slopes representing the scale factors. Different values of σ_f correspond to launch velocities 0.6–1.2 m/s, with t_{ex} between 133 and 252 ms. In all cases, $T = 52$ ms. (b) Measured scale factor for different values of σ_i and σ_f . The solid line is a linear fit with slope $-0.79(4)$, deviating from the predicted value -1 . (c) Measured fringe contrast for different values of σ_i and σ_f . The solid line is an exponential fit to $c = c_0 \exp[-\alpha \kappa^2 \sigma_i^2 / (1 - \sigma_i^2 / \sigma_f^2)]$ with $\alpha = 0.65(3)$, deviating from the model prediction $\alpha = 0.5$.

V. CONTRAST-BASED STABILIZATION

A. Model description

The first method we present for correcting scale-factor instability exploits the correlation between Ω and (κ, c, σ_f) , which are extracted from each PSI image. We obtain the relation $\Omega(\kappa, c, \sigma_f)$ by eliminating σ_i from Eqs. (1) and (2). To capture the aforementioned deviations from the model, we add a single parameter β and replace $\sigma_f \rightarrow \sigma_f/\beta$. The resulting expression for Ω is then

$$\Omega = \frac{\kappa}{F_{\text{ps}}} \left[1 - 2 \left(\frac{\beta}{\kappa \sigma_f} \right)^2 \ln \frac{c}{c_0} \right]. \quad (3)$$

As demonstrated below, we verify that this formulation, based on one physical parameter c_0 and one correction parameter β , provides an excellent description of the measured data. Importantly, it allows us to calculate Ω using only the parameters κ , c , and σ_f measured in every single PSI image, enabling analysis on a single-shot basis without any reduction in temporal bandwidth.

B. Parameter calibration

To calibrate c_0 and β in Eq. (3), we perform measurements at a constant rotation rate and periodically vary σ_i by changing the repump beam intensity during the moving optical molasses. This results in changes to c , σ_f , and κ , as shown in Fig. 4(a). Inverting Eq. (3) and setting $\Omega = \Omega_{\text{calib}}$, we obtain

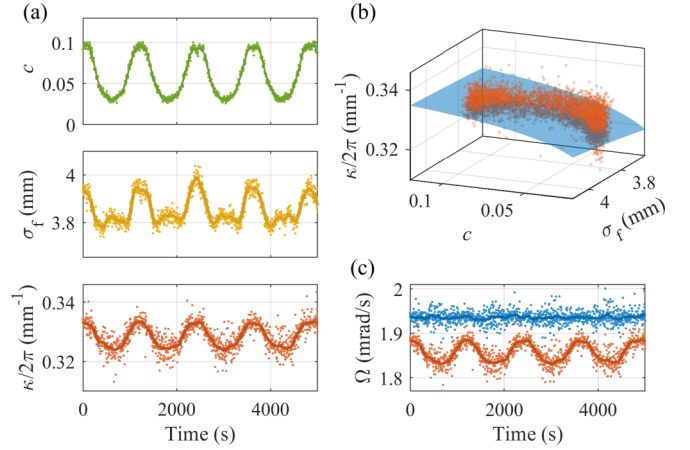


FIG. 4. Calibration of contrast-based scale-factor stabilization. (a) Top to bottom: measured contrast, final cloud size, and spatial fringe frequency for an applied rotation rate of 2 mrad/s, as σ_i is varied periodically in the range 0.5–0.8 mm. Each data point represents a single PSI image. In these and the following experiments, $T = 80$ ms and $t_{\text{ex}} = 185$ ms. (b) Parametric plot of $\kappa(c, \sigma_f)$. Dots are data points; the surface is a fit to Eq. (4) with $c_0 = 0.43(8)$ and $\beta = 0.80(1)$. The fit describes the data points well, with residuals of κ from the fit surface showing no correlation to c or σ_f and characterized by standard deviation $(2\pi)2.49 \times 10^{-3} \text{ mm}^{-1}$, consistent with a moving standard deviation $(2\pi)2.55 \times 10^{-3} \text{ mm}^{-1}$ of the raw κ measurements. (c) Rotation rate calculated with the uncorrected scale factor F_{ps} (red), compared to the corrected rotation rate (blue), which employs Eq. (3) with the calibrated parameters, showing excellent rejection of scale-factor drifts. The solid lines in (a) and (c) are 30-sample moving averages.

an expression for κ in this calibration measurement,

$$\kappa = \frac{1}{2} F_{\text{ps}} \Omega_{\text{calib}} \left[1 + \sqrt{1 + \frac{8 \ln(c/c_0)}{(F_{\text{ps}} \Omega_{\text{calib}} \sigma_f / \beta)^2}} \right]. \quad (4)$$

The measured data points are fitted to this surface equation, as shown in Fig. 4(b), where c_0 , β , and Ω_{calib} are the fit parameters, the latter being an auxiliary parameter not used in any subsequent analysis.

With calibrated c_0 and β at hand, we now use Eq. (3) to correct the inferred rotation rate in this calibration run. This exercise is shown in Fig. 4(c), and indeed we find that the drifts are removed and a stable rotation measurement is obtained. We emphasize that the analysis does not use any assumption or prior knowledge on σ_i or on its temporal variations, and in fact the only prerequisite is that the range of σ_i scanned during the calibration process is large enough to adequately calibrate the model parameters.

While this correction is aimed to improve the measurement stability under variations of σ_i , the measurement accuracy is enhanced as well. As Eq. (3) also captures the systematic bias due to the finite magnification ratio, as described by Eq. (1), applying this correction suppresses the systematic bias. Indeed, we find the postcorrection estimated rotation rate [Fig. 4(c)] to be 1.936(6) mrad/s, in agreement with the expected value 1.9387 mrad/s which consists of the applied mirror rotation rate of 2 mrad/s and the projection of the Earth's rotation on the measurement axis, which was due

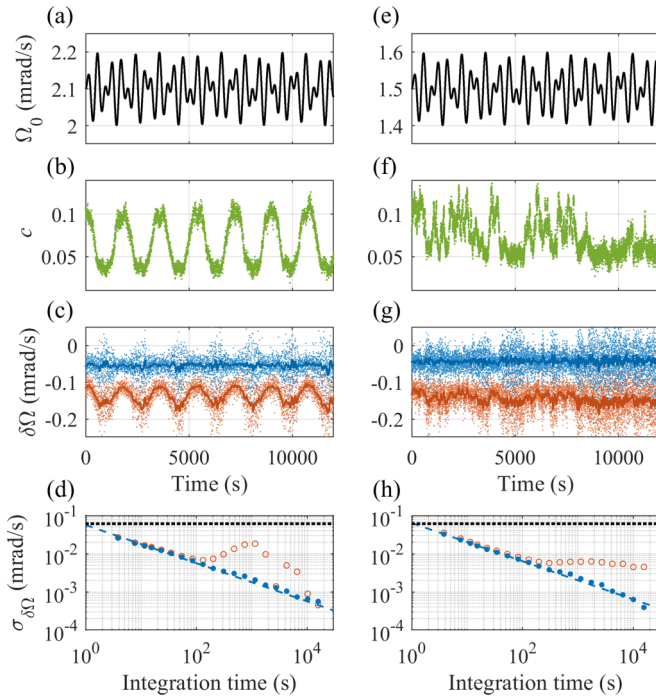


FIG. 5. Demonstration of contrast-based scale-factor stabilization. (a) Time series of the input rotation rate Ω_0 , oscillating around 2.1 mrad/s. (b) Measured fringe contrast shows variations due to applied periodic changes to σ_i . (c) Residuals of the estimated rotation rate $\Omega - \Omega_0$, with (blue) and without (red) scale-factor correction using Eq. (3). The solid lines are 30-sample moving averages. The full data spans 3×10^4 s. (d) Allan deviation of the residuals, with (filled markers) and without (empty markers) scale-factor correction. The dashed line is a fit to $\tau^{-1/2}$. The dotted line indicates the Earth's rotation rate at our laboratory location. (e)–(h) Same as (a)–(d), with Ω_0 oscillating around 1.5 mrad/s and random-walk variations in σ_i in the range 0.5–0.8 mm. The observed sensitivities are $28 \mu\text{rad/s}$ and $32 \mu\text{rad/s}$ per shot in (d) and (h), respectively, differing slightly due to changing experimental conditions, such as total atom number.

north, at our latitude of 32.7940° N. In contrast, the mean estimated rotation rate using the point-source scale factor is 1.857 mrad/s, differing significantly from the true value.

Nevertheless, it is possible that some residual bias still exists after applying Eq. (3). However, it would be inseparable from other possible sources of systematic bias in the PSI measurement due to, e.g., the effect of wavefront aberrations [25,40,41] or imaging distortions. Calibration error of the piezo stage and inaccurate estimation of the measurement axis north alignment will contribute to an apparent bias as well. For this reason Ω_{calib} is treated as a fit parameter when using Eq. (4), rather than being simply taken as the input rotation rate. The overall bias may be corrected by calibrating the PSI sensor, for example, using a precision rotary stage.

C. Demonstration of correction performance

We demonstrate the implementation of this stabilization method in two separate measurement runs, as presented in Fig. 5, representing realistic operating scenarios where the rotation rate varies in time. We artificially generate scale-factor drifts by varying the optical molasses parameters which

affect the initial and final cloud distributions, both in periodic fashion and in random-walk-like behavior. While the rotation rate and initial conditions change smoothly in time, this information is not used in the analysis as all corrections are on a single-shot basis. The interferometer parameters are $T = 80$ ms and $t_{\text{ex}} = 185$ ms, as in the calibration run.

Using Eq. (3) and the previously calibrated values for c_0 and β , we obtain suppression of sensor drifts by a factor of ten in both examples [Figs. 5(d) and 5(h)], limited only by the magnitude of the drifts we introduced. The scheme allows complete recovery of $\tau^{-1/2}$ averaging performance at timescales up to 10^4 seconds, affirming that it does not introduce new bias instabilities of its own. The second example, where Ω varies around a mean value smaller than Ω_{calib} , and the model measurements shown in Fig. 3 with larger values of Ω , demonstrate that the technique is robust and does not require multiple calibration runs with different values of Ω_{calib} . Our measurements reach a stability of $0.5 \mu\text{rad/s}$, providing an upper bound for the scale-factor stability of 2.5×10^{-4} . Under the applied variation of $\pm 18\%$ in σ_i , reaching such stability without any correction scheme would require operating the PSI sensor at a magnification ratio of at least 40.

Finally, we note that it is possible, in principle, to apply a correction similar to that described in this section by utilizing Eq. (1) and directly measuring σ_i . This may be done either in separate experimental shots, at the expense of reduced bandwidth and sensitivity per \sqrt{Hz} and under the constraint that σ_i changes little between shots, or through nondestructive imaging of the cloud during the final moving molasses stage. The latter is challenging as it requires short exposure time to avoid motion blur of the small, moving cloud. In addition to these constraints, as Fig. 3(b) demonstrates, Eq. (1) requires an additional scaling parameter to fit the measured data, likely due to the non-Gaussian shape of the initial cloud. Thus, this approach of directly measuring σ_i does not eliminate the need for calibration parameters.

VI. SELF-CALIBRATING STABILIZATION

A. Principles and demonstration

Our second method for scale-factor stabilization utilizes the piezo rotation stage to apply a known rotation Ω_{bias} at alternating measurements, in addition to the unknown rotation Ω which we wish to measure. Denoting the scale factor in these measurements as F , the spatial fringe frequencies of two consecutive measurements are given by $\kappa_1 = F\Omega$ and $\kappa_2 = F(\Omega + \Omega_{\text{bias}})$. These equations may be inverted to yield

$$\Omega = \Omega_{\text{bias}} \frac{\kappa_1}{\kappa_2 - \kappa_1}, \quad (5)$$

$$F = \frac{1}{\Omega_{\text{bias}}} (\kappa_2 - \kappa_1), \quad (6)$$

allowing us to extract both Ω and F from each pair of measurements κ_1 and κ_2 . This self-calibrating method requires no prior knowledge or assumption of a model describing the relationship between F and other system parameters. The signs of κ_1, κ_2 are not directly available from the PSI images, but rather assumed to be known, for example, from an auxiliary rotation sensor, as in all existing schemes of PSI.

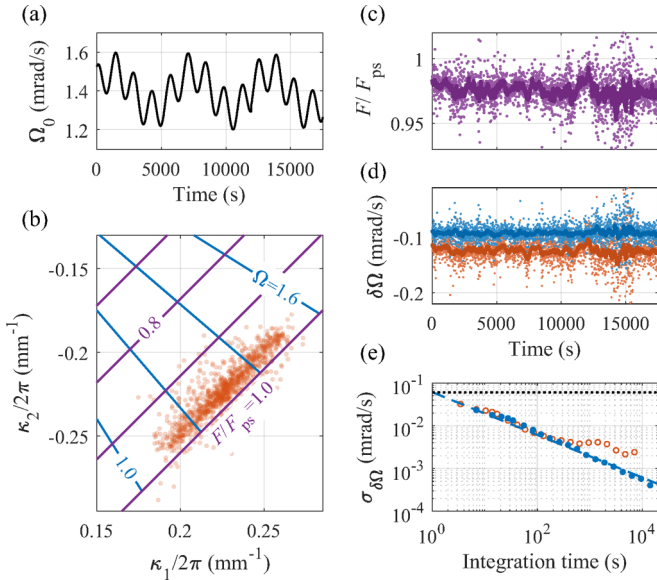


FIG. 6. Demonstration of scale-factor stabilization by self-calibration. (a) Time series of the input rotation rate Ω_0 . (b) Measured κ_2 and κ_1 , each dot corresponding to a pair of experiments with and without $\Omega_{\text{bias}} = -2.6$ mrad/s. Also shown are contour lines of the estimated rotation rate (blue) and scale-factor correction relative to F_{ps} (purple) based on Eqs. (5) and (6). (c) Estimated scale-factor correction from each pair of measurements, showing random-walk variations due to applied changes to σ_i in the range 0.5–0.8 mm. (d) Residuals of the estimated rotation rate $\Omega - \Omega_0$, using the nominal scale factor $F = F_{\text{ps}}$ (red) and the corrected scale factor (blue). The solid lines in (c) and (d) are 30-sample moving averages. (e) Allan deviation of the residuals, with and without scale-factor correction. The dashed line is a fit to $\tau^{-1/2}$ with sensitivity $32 \mu\text{rad/s}$ per shot.

An experimental demonstration of the self-calibration method is shown in Fig. 6, with both the measured rotation Ω and the scale factor changing in time. Again we find perfect suppression of scale-factor drifts and recovery of $\tau^{-1/2}$ noise behavior. Compared to the previously described contrast-based stabilization, this method reduces the effective bandwidth by a factor of two due to the pairwise analysis, but has the advantages of being model independent and not requiring any initial calibration measurements. We note that despite the reduction in bandwidth, information is not lost when analyzing pairs of measurements and thus the rotation sensitivity per $\sqrt{\text{Hz}}$ is maintained, as evident in Fig. 6(e).

This correction scheme relies on an accurate piezo stage for adding a known bias rotation, as errors in Ω_{bias} enter directly into the estimation of Ω itself. Therefore, the stage is required to have similar resolution as the PSI measurement so as not to degrade its sensitivity, and long-term stability to enable scale-factor corrections at long times. As our results show, these conditions are fulfilled in our apparatus. Indeed, such a stage with adequate performance is likely to be necessary anyway in an operational rotation sensor, for purposes such as calibration and dynamic range compensation.

B. Generalization to time-varying scenarios

The analysis above assumed that Ω and F are constant in both measurements. We now turn to the more general case

where these quantities may change between shots. We define $\Omega_1 = \Omega + \delta\Omega$, $\Omega_2 = \Omega - \delta\Omega + \Omega_{\text{bias}}$, and $F_{1,2} = F_0 + \delta F_{\text{comm}} \pm \delta F_{\text{diff}}$, such that the measured spatial fringe frequencies are $\kappa_{1,2} = F_{1,2}\Omega_{1,2}$. Here, $\delta\Omega$ represents shot-to-shot variation in Ω , F_0 is the nominal scale factor, and δF_{comm} and δF_{diff} are scale-factor errors common and different, respectively, in both measurements. Ω_{bias} , as before, is the known rotation which is added in the second measurement. Using Eq. (5) and to leading order in $\delta\Omega/\Omega$ and $\delta F/F$, we find that the estimated rotation rate is

$$\frac{\Omega_{\text{est}}}{\Omega} \approx 1 + \left(2 + \frac{2\Omega}{\Omega_{\text{bias}}}\right) \frac{\delta F_{\text{diff}}}{F_0} + \left(1 + \frac{2\Omega}{\Omega_{\text{bias}}}\right) \frac{\delta\Omega}{\Omega}. \quad (7)$$

To eliminate the $\delta\Omega$ -related term in Eq. (7), we set $\Omega_{\text{bias}} = -2(\kappa_1/F_0)$, where κ_1/F_0 corresponds to an estimate of Ω_1 based on the first measurement and assuming the nominal scale factor. With this choice of Ω_{bias} , we have, to leading order, $\Omega_{\text{est}} \approx \Omega(1 + \delta F_{\text{diff}}/F_0)$, such that the estimated rotation rate corresponds to the average Ω of the two measurements.

Regardless of the exact choice of Ω_{bias} , we find that even in this case of varying-rotation rate and scale factor, the result is insensitive to errors in the scale factor which are common to both measurements and remains sensitive only to noncommon scale-factor errors δF_{diff} . In contrast, the “naive” measurement approach, with $\Omega_{\text{bias}} = 0$ and estimating Ω as the average $\frac{1}{2}(\kappa_1 + \kappa_2)/F_0$, leads to $\Omega_{\text{naive}} \approx \Omega(1 + \delta F_{\text{comm}}/F_0)$. It is then the noncommon scale-factor error which cancels to leading order, and the common error remains.

In most scenarios, $\delta F_{\text{comm}} \gg \delta F_{\text{diff}}$, i.e., the scale factor is expected to change slowly with respect to the timescale of two measurements, and thus our self-calibrating method cancels the more dominant source of error. Additionally, more advanced estimation protocols such as a Kalman filter [42,43] could be used to track rapidly varying rotation signals while estimating the slowly varying scale factor from multiple measurement pairs.

VII. CONCLUSION

We have presented two complementary approaches for improving the stability of rotation measurements using point-source atom interferometry, suppressing scale-factor drifts which arise due to changes in the atomic cloud parameters. We demonstrated the two schemes experimentally with complete suppression of scale-factor drifts. We showed that they maintain the sensor sensitivity and do not introduce any drifts on their own. We achieved scale-factor stability on timescales up to 10^4 s, representing orders-of-magnitude improvement in stability time compared to previous works. We reach rotation rate stability of $0.5 \mu\text{rad/s}$.

The first approach utilizes the inherent correlations between different parameters in PSI images, namely, the contrast, spatial frequency, and final size of the fringe pattern, for estimating the scale factor from a single image and correct for drifts. The underlying model which describes these correlations is based on the physics of the sensor, rather than on an empirical correlation, as we verify by independent measurements. This method is based on information which is already available in standard PSI measurements and maintains the original bandwidth of the sensor; however, preliminary

calibration of two model parameters is necessary. The possibility of using a continuous estimation protocol, such as Kalman [42,43] or particle filtering [44], to replace the initial calibration as well as to allow temporal variations of these parameters may also be explored.

The second approach relies on sequential measurements with an added bias rotation to directly estimate the scale factor from each pair of measurements. This approach is self-calibrating and completely model independent, but it depends on the stability of the piezo mirror stage generating the bias rotation and reduces the sensor bandwidth.

While the experiments described here focus on side-imaging PSI which allows single-axis rotation sensing, the two schemes that we developed are fully compatible under the same conditions with dual-axis sensors using top or bottom imaging of the cloud.

The stabilization techniques that we developed are particularly important in compact PSI sensors, which are an attractive

alternative for constructing simple, mobile devices with high sensitivity to rotations. Our schemes address a significant challenge of such PSI sensors, namely, high susceptibility to scale-factor drifts due to the low magnification ratio of the atomic cloud. The results may pave the way for realizing high-performance, compact PSI devices for demanding applications that require long-time stability, such as gyrocompasses for north-finding applications, gyroscopes for line-of-sight stabilization, or inertial measurement units for navigation systems.

ACKNOWLEDGMENTS

This work was supported by the Pazy Foundation, the Israel Science Foundation, and the Quantum Technologies Development Consortium (RA). We thank Shlomi Kotler for fruitful discussions.

-
- [1] Atom Interferometry, in *Proceedings of the International School of Physics "Enrico Fermi," Course CLXXXVIII*, edited by G. M. Tino and M. A. Kasevich (Societa Italiana di Fisica and IOS Press, Amsterdam, 2014).
- [2] D. S. Weiss, B. C. Young, and S. Chu, Precision Measurement of the Photon Recoil of an Atom Using Atomic Interferometry, *Phys. Rev. Lett.* **70**, 2706 (1993).
- [3] S. Dimopoulos, P. W. Graham, J. M. Hogan, and M. A. Kasevich, Testing General Relativity with Atom Interferometry, *Phys. Rev. Lett.* **98**, 111102 (2007).
- [4] H. Müller, A. Peters, and S. Chu, A precision measurement of the gravitational redshift by the interference of matter waves, *Nature (London)* **463**, 926 (2010).
- [5] R. Bouchendira, P. Cladé, S. Guellati-Khélifa, F. Nez, and F. Biraben, New Determination of the Fine Structure Constant and Test of the Quantum Electrodynamics, *Phys. Rev. Lett.* **106**, 080801 (2011).
- [6] G. Rosi, F. Sorrentino, L. Cacciapuoti, M. Prevedelli, and G. M. Tino, Precision measurement of the newtonian gravitational constant using cold atoms, *Nature (London)* **510**, 518 (2014).
- [7] L. Zhou, S. Long, B. Tang, X. Chen, F. Gao, W. Peng, W. Duan, J. Zhong, Z. Xiong, J. Wang, Y. Zhang, and M. Zhan, Test of Equivalence Principle at 10⁻⁸ Level by a Dual-Species Double-Diffraction Raman Atom Interferometer, *Phys. Rev. Lett.* **115**, 013004 (2015).
- [8] B. Barrett, L. Antoni-Micollier, L. Chichet, B. Battelier, T. Lévêque, A. Landragin, and P. Bouyer, Dual matter-wave inertial sensors in weightlessness, *Nat. Commun.* **7**, 13786 (2016).
- [9] R. H. Parker, C. Yu, W. Zhong, B. Estey, and H. Müller, Measurement of the fine-structure constant as a test of the standard model, *Science* **360**, 191 (2018).
- [10] D. Becker, M. D. Lachmann, S. T. Seidel, H. Ahlers, A. N. Dinkelaker, J. Grosse, O. Hellmig, H. Müntinga, V. Schkolnik, T. Wendrich, A. Wenzlawski, B. Weps, R. Corgier, T. Franz, N. Gaaloul, W. Herr, D. Lüdtke, M. Popp, S. Amri, H. Duncker, M. Erbe, A. Kohfeldt, A. Kubelka-Lange, C. Braxmaier, E. Charron, W. Ertmer, M. Krutzik, C. Lämmerzahl, A. Peters, W. P. Schleich, K. Sengstock, R. Walser, A. Wicht, P. Windpassinger, and E. M. Rasel, Space-borne Bose-Einstein condensation for precision interferometry, *Nature (London)* **562**, 391 (2018).
- [11] K. Bongs, M. Holynski, J. Vovrosh, P. Bouyer, G. Condon, E. Rasel, C. Schubert, W. P. Schleich, and A. Roura, Taking atom interferometric quantum sensors from the laboratory to real-world applications, *Nat. Rev. Phys.* **1**, 731 (2019).
- [12] X. Wu, Gravity gradient survey with a mobile atom interferometer, Ph.D. thesis, Stanford University, 2009.
- [13] T. Farah, C. Guerlin, A. Landragin, Ph. Bouyer, S. Gaffet, F. P. Dos Santos, and S. Merlet, Underground operation at best sensitivity of the mobile LNE-SYRTE cold atom gravimeter, *Gyroscop. Navigat.* **5**, 266 (2014).
- [14] C. Freier, M. Hauth, V. Schkolnik, B. Leykauf, M. Schilling, H. Wziontek, H.-G. Scherneck, J. Müller, and A. Peters, Mobile quantum gravity sensor with unprecedented stability, *J. Phys. Conf. Ser.* **723**, 012050 (2016).
- [15] V. Ménotret, P. Vermeulen, N. Le Moigne, S. Bonvalot, P. Bouyer, A. Landragin, and B. Desruelle, Gravity measurements below 10⁻⁹ g with a transportable absolute quantum gravimeter, *Sci. Rep.* **8**, 12300 (2018).
- [16] Y. Bidel, N. Zahzam, C. Blanchard, A. Bonnin, M. Cadoret, A. Bresson, D. Rouxel, and M. F. Lequentrec-Lalancette, Absolute marine gravimetry with matter-wave interferometry, *Nat. Commun.* **9**, 627 (2018).
- [17] X. Wu, Z. Pagel, B. S. Malek, T. H. Nguyen, F. Zi, D. S. Scheirer, and H. Müller, Gravity surveys using a mobile atom interferometer, *Sci. Adv.* **5**, eaax0800 (2019).
- [18] Y. Bidel, N. Zahzam, A. Bresson, C. Blanchard, M. Cadoret, A. V. Olesen, and R. Forsberg, Absolute airborne gravimetry with a cold atom sensor, *Science* **360**, 191 (2018).
- [19] B. Barrett, R. Geiger, I. Dutta, M. Meunier, B. Canuel, A. Gauguier, P. Bouyer, and A. Landragin, The Sagnac effect: 20 years of development in matter-wave interferometry, *C. R. Phys.* **15**, 875 (2014).
- [20] T. L. Gustavson, P. Bouyer, and M. A. Kasevich, Precision Rotation Measurements with an Atom Interferometer Gyroscope, *Phys. Rev. Lett.* **78**, 2046 (1997).

- [21] J. K. Stockton, K. Takase, and M. A. Kasevich, Absolute Geodetic Rotation Measurement using Atom Interferometry, *Phys. Rev. Lett.* **107**, 133001 (2011).
- [22] S. M. Dickerson, J. M. Hogan, A. Sugarbaker, D. M. S. Johnson, and M. A. Kasevich, Multiaxis Inertial Sensing with Long-Time Point Source Atom Interferometry, *Phys. Rev. Lett.* **111**, 083001 (2013).
- [23] D. Savoie, M. Altorio, B. Fang, L. A. Sidorenkov, R. Geiger, and A. Landragin, Interleaved atom interferometry for high-sensitivity inertial measurements, *Sci. Adv.* **4**, eaau7948 (2018).
- [24] Y.-J. Chen, A. Hansen, G. W. Hoth, E. Ivanov, B. Pelle, J. Kitching, and E. A. Donley, Single-Source Multiaxis Cold-Atom Interferometer in a Centimeter-Scale Cell, *Phys. Rev. Appl.* **12**, 014019 (2019).
- [25] A. Gauguet, B. Canuel, T. Lévêque, W. Chaibi, and A. Landragin, Characterization and limits of a cold-atom Sagnac interferometer, *Phys. Rev. A* **80**, 063604 (2009).
- [26] A. Sugarbaker, S. M. Dickerson, J. M. Hogan, D. M. S. Johnson, and M. A. Kasevich, Enhanced Atom Interferometer Readout through the Application of Phase Shear, *Phys. Rev. Lett.* **111**, 113002 (2013).
- [27] C. Jekeli, Navigation error analysis of atom interferometer inertial sensor, *Navigation* **52**, 1 (2005).
- [28] B. Canuel, F. Leduc, D. Holleville, A. Gauguet, J. Fils, A. Virdis, A. Clairon, N. Dimarcq, C. J. Bordé, A. Landragin, and P. Bouyer, Six-Axis Inertial Sensor Using Cold-Atom Interferometry, *Phys. Rev. Lett.* **97**, 010402 (2006).
- [29] A. V. Rakholia, H. J. McGuinness, and G. W. Biedermann, Dual-Axis High-Data-Rate Atom Interferometer Via Cold Ensemble Exchange, *Phys. Rev. Appl.* **2**, 054012 (2014).
- [30] D. S. Durfee, Y. K. Shaham, and M. A. Kasevich, Long-Term Stability of an Area-Reversible Atom-Interferometer Sagnac Gyroscope, *Phys. Rev. Lett.* **97**, 240801 (2006).
- [31] H. C. Lefèvre, *The Fiber-Optic Gyroscope* (Artech House, London, 2014).
- [32] B. Battelier, B. Barrett, L. Fouché, L. Chichet, L. Antonimiccollier, H. Porte, F. Napolitano, J. Lautier, A. Landragin, and P. Bouyer, Development of compact cold-atom sensors for inertial navigation, in *Quantum Optics*, edited by J. Stuhler and A. J. Shields (SPIE, Brussels, Belgium, 2016).
- [33] G. W. Hoth, B. Pelle, S. Riedl, J. Kitching, and E. A. Donley, Point source atom interferometry with a cloud of finite size, *Appl. Phys. Lett.* **109**, 071113 (2016).
- [34] G. W. Hoth, B. Pelle, J. Kitching, and E. A. Donley, Analytical tools for point source interferometry, in *Slow Light, Fast Light, and Opto-Atomic Precision Metrology X*, edited by S. M. Shahriar and J. Scheuer (SPIE, San Francisco, California, United States, 2017).
- [35] M. Kasevich and S. Chu, Atomic Interferometry Using Stimulated Raman Transitions, *Phys. Rev. Lett.* **67**, 181 (1991).
- [36] M. Kasevich, D. S. Weiss, E. Riis, K. Moler, S. Kasapi, and S. Chu, Atomic Velocity Selection Using Stimulated Raman Transitions, *Phys. Rev. Lett.* **66**, 2297 (1991).
- [37] D. Yankelev, C. Avinadav, N. Davidson, and O. Firstenberg, Multiport atom interferometry for inertial sensing, *Phys. Rev. A* **100**, 023617 (2019).
- [38] C. Avinadav, D. Yankelev, O. Firstenberg, and N. Davidson, Composite-Fringe Atom Interferometry for High Dynamic-Range Sensing, *Phys. Rev. Appl.* **13**, 054053 (2020).
- [39] H. C. Lefèvre, The fiber-optic gyroscope, a century after Sagnac's experiment: The ultimate rotation-sensing technology? *C. R. Phys.* **15**, 851 (2014).
- [40] V. Schkolnik, B. Leykauf, M. Hauth, C. Freier, and A. Peters, The effect of wavefront aberrations in atom interferometry, *Appl. Phys. B* **120**, 311 (2015).
- [41] R. Karcher, A. Imanaliev, S. Merlet, and F. P. Dos Santos, Improving the accuracy of atom interferometers with ultracold sources, *New J. Phys.* **20**, 113041 (2018).
- [42] R. E. Kalman, A new approach to linear filtering and prediction problems, *J. Basic Engineer.* **82**, 35 (1960).
- [43] P. Cheiney, L. Fouché, S. Templier, F. Napolitano, B. Battelier, P. Bouyer, and B. Barrett, Navigation-Compatible Hybrid Quantum Accelerometer Using a Kalman Filter, *Phys. Rev. Appl.* **10**, 034030 (2018).
- [44] P. Del Moral, Nonlinear filtering: Interacting particle resolution, *C. R. Acad. Sci., Ser. I, Math.* **325**, 653 (1997).